UC San Diego
UC San Diego Previously Published Works

Title

Wide Potential Window Supercapacitors Using Open-Shell Donor–Acceptor Conjugated Polymers with Stable N-Doped States

Permalink

https://escholarship.org/uc/item/8f68v81f

Journal

Advanced Energy Materials, 9(47)

ISSN

1614-6832

Authors

Wang, Kaiping
Huang, Lifeng
Eedugurala, Naresh
et al.

Publication Date

2019-12-01

DOI

10.1002/aenm.201902806

Peer reviewed

Wide Potential Window Supercapacitors Using Open-Shell Donor–Acceptor Conjugated Polymers with Stable N-Doped States

Kaiping Wang, Lifeng Huang, Naresh Eedugurala, Song Zhang, Md Abdus Sabuj, Neeraj Rai, Xiaodan Gu, Jason D. Azoulay, and Tse Nga Ng*

Supercapacitors have emerged as an important energy storage technology offering rapid power delivery, fast charging, and long cycle lifetimes. While extending the operational voltage is improving the overall energy and power densities, progress remains hindered by a lack of stable n-type redox-active materials. Here, a new Faradaic electrode material comprised of a narrow bandgap donor–acceptor conjugated polymer is demonstrated, which exhibits an open-shell ground state, intrinsic electrical conductivity, and enhanced charge delocalization in the reduced state. These attributes afford very stable anodes with a coulombic efficiency of 99.6% and that retain 90% capacitance after 2000 charge–discharge cycles, exceeding other n-dopable organic materials. Redox cycling processes are monitored in situ by optoelectronic measurements to separate chemical versus physical degradation mechanisms. Asymmetric supercapacitors fabricated using this polymer with p-type PEDOT:PSS operate within a 3 V potential window, with a best-in-class energy density of 30.4 Wh kg^{-1} at a 1 A g^{-1} discharge rate, a power density of 14.4 kW kg^{-1} at a 10 A g^{-1} discharge rate, and a long cycle life critical to energy storage and management. This work demonstrates the application of a new class of stable and tunable redox-active material for sustainable energy technologies.

1. Introduction

Supercapacitors are electrochemical energy storage devices that store charge through fast, reversible redox reactions, enable load-leveling, regenerative energy harvesting, and high power applications.[1–6] The energy density of a supercapacitor ($E = CV^2/2$) is linearly dependent on the specific capacitance C and proportional to the square of the operational voltage V. The main strategies to increase energy depend upon the mechanism of charge storage, whether capacitive or Faradaic. Capacitive electrodes store charge on the surface; hence, research is focused on strategies to increase the surface area, typically based on high surface area carbons.[7–9] Faradaic materials undergo redox reactions and offer the ability to tune the operating voltage. There has been considerable success in tuning the cathode voltage and delivering high capacitance systems operating at the upper limit of prototypical nonaqueous electrolytes.[1,7] However, the device voltage and energy remain limited by a lack of complementary high power electrodes for the anode.[10,11] In the absence of new high voltage electrolytes, there is no room to further extend the cathode potential, because over-potential may lead to hazardous runaway reactions between the highly oxidized cathodes and flammable nonaqueous electrolytes. In contrast, it is generally safe for nonaqueous electrolytes to operate down to −2 V relative to the Ag/AgCl electrode, and the development of anode materials is critical to increase the energy densities of supercapacitors.

Consequently, there is an urgent need for strategies aimed at extending the operational voltage toward negative potentials to improve the energy density and cell voltage of supercapacitors. As an alternative to metal oxides, redox-active macromolecules offer mechanical flexibility, low-cost, and scalability relevant for small and large scale applications.[12–16] In radical polymers,[17–20] the redox sites are at pendant radical groups distributed along a polymer backbone. Due to the insulating nature of the backbone and low conductivity, devices based on these materials require blending with additional conductive materials for electron transport, ultimately lowering the electrode energy

K. Wang, Prof. T. N. Ng
Materials Science Engineering Program and Department of Electrical
and Computer Engineering
University of California San Diego
La Jolla, CA 92093, USA
E-mail: tnn046@ucsd.edu
L. Huang, N. Eedugurala, S. Zhang, Prof. X. Gu, Prof. J. D. Azoulay
Center for Optoelectronic Materials and Devices
School of Polymer Science and Engineering
The University of Southern Mississippi
Hattiesburg, MS 39406, USA
M. A. Sabuj, Prof. N. Rai
Dave C. Swalm School of Chemical Engineering and Center for Advanced
Vehicular Systems
Mississippi State University
Mississippi State, Starkville, MS 39762, USA

ADVANCED
SCIENCE NEWS
www.advancedsciencenews.com

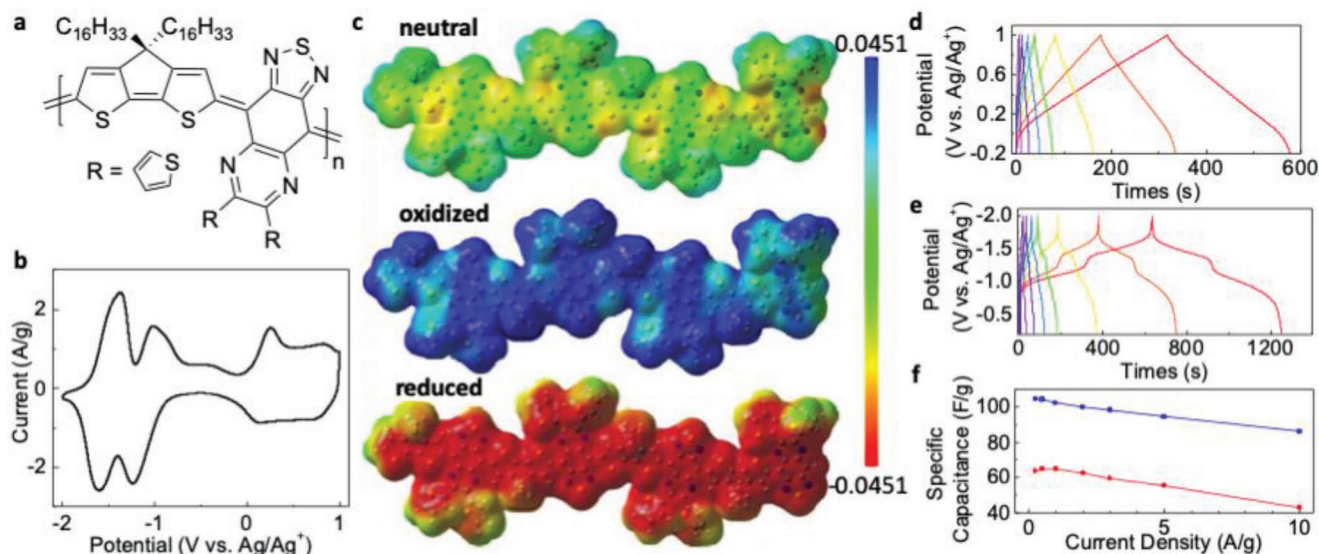**ADVANCED**
ENERGY
MATERIALS
www.advenergymat.de

Figure 1. a) Chemical structure of the open-shell donor–acceptor polymer PCQTh. b) Cyclic voltammetry at a scan rate of 10 mV s⁻¹. c) Molecular electrostatic potential map, as an isosurface for the total electron density. The blue and red surface represents the highest (fewer electrons) and lowest (more electrons) electrostatic potential, respectively. The color scale is in units of Hartree. Galvanostatic charge–discharge measurements of PCQTh as d) a cathode and e) an anode in three-electrode configuration, at current densities of 0.25, 0.5, 1, 2, 3, 5, and 10 A g⁻¹ (red to purple). f) Specific capacitance versus current densities of the cathode (red) and anode (blue).

density.[17] Conjugated polymers that were n-doped as the negative electrode[21–26] have also been explored, but the high charge transfer resistance negatively impacts the performance, and rapid degradation occurs due to instability associated with strong charge localization. The relatively localized redox states can be attributed to the inherent disorder in these materials. Overall, the aforementioned technologies lead to poor coulombic efficiency and rapid degradation with redox cycling, exhibiting a low capacitance retention of <80% at 1000 cycles.[25,27]

Here, we examine a new approach to meet the critical need for stable Faradaic anodes through the use of an open-shell donor–acceptor (DA) conjugated polymer (CP) with intrinsic electrical conductivity ($\sigma \approx 10^{-3}$ S cm⁻¹) and enhanced charge delocalization in the reduced state. We recently demonstrated a novel class of DA CPs[28] with very narrow bandgaps and open-shell electronic structures emanating from a high degree of electronic coherence along the conjugated backbone, despite inherent disorder and heterogeneity. Salient molecular design features include a cyclopentadithiophene donor and a proquinoidal thiophene-substituted thiadiazoloquinoxaline acceptor, which collectively promote strong π-electron correlations, extensive delocalization, a very narrow bandgap, and form and stabilize unpaired spins in the long-chain (polymer) limit. The intrinsic instability of open-shell materials has traditionally limited their practical implementation into devices, owing to their electron-rich nature and highly localized radical sites. In our polymer, there is significant internal charge transfer character between electron-rich (donor) and electron-deficient (acceptor) components throughout the π-framework and extensive delocalization of the spin density, a requisite for high conductivity and thermodynamic stabilization. Furthermore, the polymer is highly soluble in organic solvents and can be processed by solution

deposition approaches, rendering it more versatile and scalable than other molecular materials that are electropolymerized.

Symmetric and asymmetric supercapacitors[4] were fabricated to characterize the device energy and power densities and cycling stability over a 3 V window, such that the anodes are tested in the substantial negative range down to −2 V versus an Ag/Ag⁺ reference electrode. As the polymer shows electrochromism, we combine current–voltage and optoelectronic measurements[29] to determine the coloration efficiency and infer factors that affect capacitance retention upon redox cycling. These results, for the first time, demonstrate the potential of open-shell DA conjugated structures in overcoming the key reliability bottleneck in redox supercapacitor, for developing next-generation stable n-type electrodes.

2. Results and Discussion

2.1. Synthesis and Solid-State Electrochemical Properties

Figure 1 displays the chemical structure and redox properties of poly(4-(4,4-dihexadecyl-4*H*-cyclopenta[2,1-*b*:3,4-*b′*]dithiophen-2-yl)-6,7-di(thiophen-2-yl)-[1,2,5]thiadiazolo[3,4-*g*]quinoxaline) (PCQTh). The polymer was synthesized using a rapid microwave-assisted Stille cross-coupling copolymerization using Pd(PPh₃)₄ as the catalyst. A reaction time of 1 h 20 min afforded the polymer in 79% yield following purification using Soxhlet extraction (See the Supporting Information for full details). This rapid and modular polymerization approach overcomes a significant synthetic challenge since it allows for the synthesis of stable, highly π-conjugated, open-shell polymers with very narrow bandgaps. This contrasts with previous classes of open-shell materials, largely focused on

small molecules and oligomers, which require protracted and multistep synthetic approaches, are largely unstable, and limited in their applicability. Furthermore, a diversity of structure and electronic features can be readily explored through using various comonomers.

Cyclic voltammetry (CV) shows that the highest occupied molecular orbital (HOMO) is located at −4.95 eV and the lowest unoccupied molecular orbital (LUMO) at −4.15 eV, which gives an electrochemical bandgap (E_g^{elec}) of 0.80 eV. The charge-neutral PCQTh exhibits intrinsic electrical conductivity of ≈10^{-3} S cm^{-1} in the absence of dopants (conductivity and electrochemical impedance data are included in Figure S1 in the Supporting Information). CV of the PCQTh film shows two redox peaks in the negative potential range, indicating there are two electron-transfer processes between 0 and −2 V (Figure 1b). A high degree of charge delocalization throughout the polymer chain is predicted by molecular orbital calculations of spin densities in Figure 1c (computational details included in the Supporting Information). When the polymer is oxidized or reduced, there were no distinct redox sites, and only a slight increase of positive charge density on the donor and negative charge density on the acceptor unit. Overall, extensive π-conjugation is maintained as seen in the molecular electrostatic maps of the neutral, oxidized, and reduced states.

It was recently demonstrated that electronic states in this class of polymers can be tuned from closed-shell singlets to biradicaloids with varying amounts of open-shell character, to biradicals in singlet and triplet spin states.[28,30] Electron spin resonance spectra, collected at room temperature, shows a well-defined signal at $g_e = 2.006$, indicating unpaired or weakly paired electrons (Figure S2, Supporting Information). These results are consistent with density functional theory (DFT) calculations at the unrestricted (U)B3LYP/6–31+G** level of theory and basis set on an oligomer with four repeat units ($n = 4$). The contribution of the open-shell resonance form to the ground state is described by the diradical character index ($0 < \gamma < 1$), with $\gamma = 1$ implying the formation of a pure diradical. PCQTh shows $\gamma = 0.62$ at $n = 4$, which indicates significant diradical character in the ground state, even at low conjugation lengths.

In Figure 1d,e, PCQTh films are characterized by the galvanostatic charge–discharge (GCD) method in a three-electrode configuration, to measure the specific capacitance at various current densities and voltage ranges. The capacitance C is calculated from the relation[31,32] $C = I/(dV/dt)$,

where I is the discharge current, and dV/dt is the derivative of voltage with respect to time. The specific capacitance in Figure 1f is the measured capacitance divided by the mass of PCQTh films. The influence of the active material loading is shown in Figure S1f in the Supporting Information, and currently the optimal loading is around 2 mg cm^{-2}. When the polymer is tested as an anode, it is cycled between −0.2 and −2 V and ranges from 104 to 90 F g^{-1} for current densities of 0.25–10 A g^{-1}. The theoretical pseudocapacitance for the anode is 112 F g^{-1}, which is calculated from the equation[33] $C_{pse} = (n \times F)/(3.6 \times M)$, in which n is number of electrons involved into the reaction, F is farad constant, and M is the molecular weight. As a cathode, the polymer shows irreversible reactions beyond 1 V, and therefore the GCD characterization is limited between −0.2 and 1 V. In this potential range the corresponding specific capacitance ranges from 65 to 40 F g^{-1} for the cathode. The specific capacitance of the cathode and anode decreases with higher discharge current density, as is typical for redox-active electrodes. Nonetheless, they maintain at least 80% of its capacitance even when the current density is as large as 5 A g^{-1}.

The PCQTh films on carbon current collectors are assembled into a symmetric supercapacitor submerged in a nonaqueous electrolyte consisting of 0.5 M tetraethylammonium tetrafluoroborate (TEABF$_4$) in propylene carbonate (PC). Each cathode and anode pair should have equal capacity to maximize charge transfer, and so the mass loading is adjusted for each electrode based on the specific capacitance in the operational voltage range. The charge capacity $Q = CV$ is calculated as follows based on information from Figure 1f: for the anode with 104 F g^{-1} operating between −0.2 and −2 V, the capacity is $Q_{anode} = mass_{anode} \times (104$ F g$^{-1})(1.8$ V); for the cathode with 65 F g^{-1} operating between −0.2 and 1 V, $Q_{cathode} = mass_{cathode} \times (65$ F g$^{-1})(1.2$ V). In order for $Q_{anode} = Q_{cathode}$, $mass_{cathode}/mass_{anode}$ is designed to be 2.4. CV at different scan ranges and scan rates for the symmetric device are included in Figures S3 and S4 in the Supporting Information, respectively, and the CV also characterizes charge trapping effects in the electrodes. The symmetric supercapacitor in **Figure 2**b is cycled over a 3 V potential window in the two-electrode configuration. To separate the extent of redox cycling degradation in each electrode, we monitor the potential change between the electrodes in the full device (black lines) and simultaneously track the anode potential (blue lines) with respect to a nearby reference
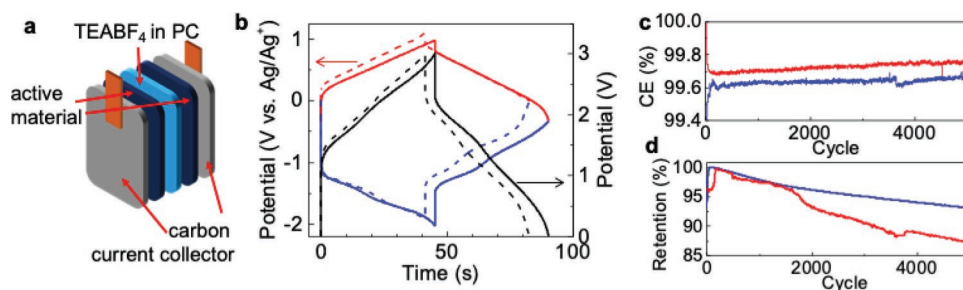

Figure 2. a) Schematic of a supercapacitor. b) Galvanostatic charge–discharge measurements of the symmetric PCQTh supercapacitor operating at a current density of 1 A g^{-1}. The solid lines are measured in cycle 1 and dashed lines in cycle 5000. The black curves are from the two-electrode configuration. Anode (blue) and cathode (red) voltage are recorded simultaneously with respect to an Ag/Ag$^+$ reference electrode submerged in the electrolyte. c) Coulombic efficiency and d) capacitance retention versus redox cycles. Similar to part (b), the blue line represents an anode cycled between −0.2 and −2 V, and the red line represents a cathode cycled between −0.2 and 1 V in three-electrode configuration.

ADVANCED
SCIENCE NEWS
www.advancedsciencenews.com

ADVANCED
ENERGY
MATERIALS
www.advenergymat.de

electrode submerged in the electrolyte. The cathode characteristics (red lines) are then inferred from the potential difference between the full device and the anode.

The supercapacitor shows excellent cycling stability. Figure 2c shows the electrodes' coulombic efficiency to be above 99.6% over 5000 redox cycles. The coulombic efficiency is the ratio of the output charge to the input charge in a charge–discharge cycle, and the high value in PCQTh electrodes indicates excellent redox reversibility and is unique among n-type materials. The PCQTh polymer performs better as an anode than a cathode, and later we will improve device performance in Section 4 by modifying the cathode material. After 5000 cycles at room temperature, the anode retains 93% of its initial capacitance as seen in Figure 2d, which showcases this polymer to be one of the most stable redox-active n-type electrodes.

2.2. Optoelectronic Properties

While PCQTh is practically stable, it may be further improved by understanding the origins of the capacitance loss after redox cycling. We studied the electrodes in situ by optical and morphological measurements to investigate possible chemical changes and structural modifications. Thin films of polymer were spin-coated onto a transparent indium tin oxide (ITO) electrode. As PCQTh is reduced, the change in carrier density shifts the near-infrared absorption of the film/polymer to visible wavelengths, as displayed in **Figure 3**. The color of the polymer is tan/beige in oxidized and neutral states. Then as the reduction proceeds, the color changes to dark blue at −2 V.
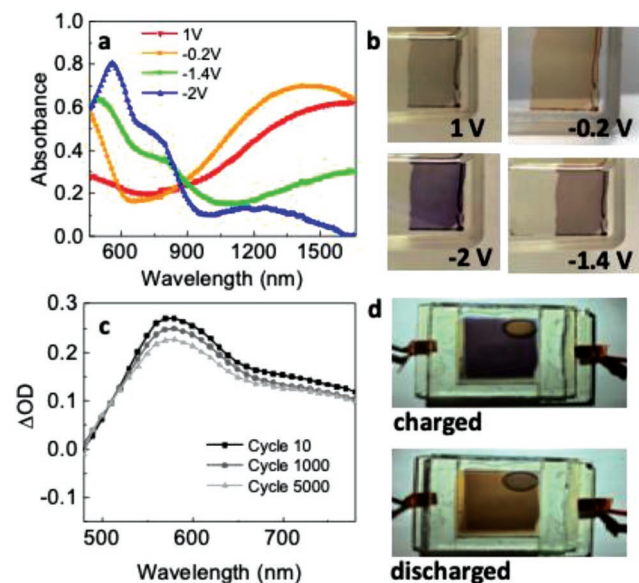

Figure 3. a) Optical absorption spectra and b) photographs of PCQTh films at various bias voltages with respect to Ag/Ag+ reference. c) Optical density versus transmitted light wavelength. The film is biased at −0.2 V for the discharged state and at −2 V for the charged state. d) Photographs of electrochromic switching in a symmetric supercapacitor when it is fully charged or discharged. As there is no electrolyte in the air bubble on the upper right corner, this part of the film does not undergo redox, and its color remains unchanged.

We leverage this electrochromic effect and determine the coloration efficiency,[34,35] which can be an indicator of unintentional side reactions during redox cycling. The coloration efficiency is the ratio of the change in optical transmission normalized to the number of electrons transferred in a charge–discharge cycle. In our films with capacitance degradation, there can be two scenarios: the transmission is changing (1) less per electron or (2) the same amount per electron. The first case with less absorption shift would imply that the electrochromic entities are chemically modified due to irreversible reactions, which would in turn lower the electrode capacitance. The second case with the same optical change would imply that the polymer remains the same. However, the film may still lose capacitance and the associated color change from fewer electrons being transferred, probably because of electrical disconnections (namely, portions of the film physically separated or becoming electrically isolated). The combination of optical and current measurements allows us to distinguish between chemical versus physical degradation.

In Figure 3c, the optical density at a specific wavelength λ is $\Delta OD(\lambda) = \log(\%T_{discharged}/\%T_{charged})$, where $\%T_{discharged}$ and $\%T_{charged}$ are the film transmission at −0.2 V and at −2 V, respectively. The percentage transmittance change ($\%\Delta T = \%T_{discharged} - \%T_{charged}$) is shown in Figure S5a in the Supporting Information. The ΔOD is the transmission ratio between the discharged neutral state and the fully charged state, and it peaks at $\lambda = 580$ nm. The optical response time in the ΔOD measurement is shown in Figure S5b in the Supporting Information, in which the optical switching time is around 1.2–1.5 s. The injected charge $Q_{electrochromic}$ is the measured current density integrated over the charging time. Finally, the coloration efficiency is found by $\Delta OD(\lambda)/Q_{electrochromic}$. The coloration efficiency is calculated in **Table 1** at the end of redox cycle #10, 1000, and 5000.

Before and after capacitance loss, the coloration efficiencies are the same within error and fit to scenario 2 as discussed above. While the electrochromic $\%\Delta T$ contrast decreased by 10%, the corresponding number of injected charges also decreased, leading to the no significant change in the coloration efficiency between cycle 10 and 5000. The electrochromic characteristics are used as a visual state-of-charge indicator, but the highly reversible color changes are also attractive for applications such as electrochromic windows and signage. We also measured the Fourier transform infrared (FTIR) spectra shown in Figure S5c in the Supporting Information, and there is a negligible difference between the spectra at cycle 10 and 1000, in agreement with the electrochromic results. Thus both the electrochromic and FTIR analyses rule out significant irreversible chemical changes as the dominant degradation mechanism.

Table 1. Electrochromic properties under redox cycling.

	Injected charge [mC cm−2]	Optical density ΔOD at 580 nm	Coloration efficiency [cm² C−1]
Cycle 10	2.25 ± 0.07	0.270	119 ± 3.8
Cycle 1000	2.05 ± 0.05	0.248	121.1 ± 2.9
Cycle 5000	1.95 ± 0.05	0.226	116.0 ± 3.0

**ADVANCED
SCIENCE NEWS**

www.advancedsciencenews.com

**ADVANCED
ENERGY
MATERIALS**

www.advenergymat.de

2.3. Morphological Changes Under Redox Cycling

During redox cycling, counter ions move to maintain charge balance in the electrodes, and solvent moves into or out of the film, which induces polymer rearrangement in response to new charge sites. Since structural changes are expected in the polymer due to repeated redox-induced expansion and contraction,[4,36–38] we examine the electrode film structure in relation to its performance. Scanning electron microscopy (SEM) is employed to morphologically investigate the PCQTh film drop-casted on a carbon paper current collector (**Figure 4**). Comparing the pristine film at cycle 0 to the film after it has been subjected to ten redox cycles, there are cracks due to the volume change between discharged and charged states of the polymer. Nonetheless, the cracks are not detrimental, because the electrode capacitance rises by 40% during this "conditioning" phase of ten cycles (Figure S6, Supporting Information). The cracks increase the surface area and allow the electrolyte counter ions to penetrate deeply into the bulk.

At the molecular level, the PCQTh film loses crystallinity after the first ten redox cycles, as seen in the grazing incidence wide-angle X-ray scattering (GIWAXS) measurements in Figure 4b. The alkyl chain stacking peaks (100) at $q = 0.27$ Å^{-1} ($d = 23.3$ Å) and (200) at $q = 0.54$ Å^{-1} ($d = 11.6$ Å) in the pristine film are no longer observable in the cycled film because the film becomes amorphous by the tenth cycle. The scattering signal at $q = 1.1$ Å^{-1} is not inherent to the polymer but rather corresponds to ionic crystal residues from the electrolyte (scattering data of a dried electrolyte sample is included in Figure S7 in the Supporting Information). While there is no noticeable change in the polymer structure between cycle 10 and 1000 across GIWAXS measurements, the average film thickness is observed to increase at the mesoscale in Figure 4c. The polymer is spin-coated onto a smooth ITO electrode, and after 1000 redox cycles, the film thickness nearly doubles, as the polymer swells with the movement of the electrolyte in and out of the film. When a pristine sample is soaked for the same amount of time without any voltage bias, the swelling is less pronounced, and film thicknesses increase by only 6%.

The morphological analysis suggests that structural changes are a factor contributing to long-term capacitance loss. The decline of the PCQTh charge retention capacity is slow and not a sudden, catastrophic failure. The cyclic volume change and swelling may lead to small portions of the polymer being gradually delaminated or electrically disconnected from the current collector. Previous research to enhance supercapacitor stability include strategies to process the redox-active materials into hierarchical structures[7,8,36] and accommodate dimensional changes.[39] Likewise these approaches can be applied to improve our future devices.

2.4. Power and Energy Densities

A symmetric supercapacitor uses the same redox-active material for both the cathode and the anode. On the other hand, asymmetric supercapacitors consist of different active materials for each electrode.[10] As displayed in Figure 1f, the specific capacitance of PCQTh is worse in the positive than in the negative voltage range, and more mass is needed in the cathode to match the anode charge capacity in the symmetric supercapacitor. Instead, we can make asymmetric devices and choose another high specific capacitance material for the cathode, to increase the capacity and benefit the overall supercapacitor performance. **Figure 5**a,b shows electrical characterization of an asymmetric supercapacitor with poly(3,4-ethylenedioxythiophene):poly(styrenesulfonate) (PEDOT:PSS) as the cathode and PCQTh as the anode. The mass ratio of cathode-to-anode is 1:1. As a p-type material, PEDOT:PSS shows excellent cycling stability[40] and similar specific capacitance (103 F g^{-1}) as PCQTh. However, PEDOT:PSS is unstable in the negative voltage range where PCQTh excels. Figure 5c compares the capacitance retention of asymmetric and symmetric devices. After 5000 redox cycles at 25 °C, the asymmetric supercapacitor shows 85% capacitance retention, while the symmetric one shows 79% retention. Figure 5d compares the capacitance retention of supercapacitors with n-type polymers, and the devices here demonstrate state-of-the-art cycle life.

Figure 5e compares the energy and power densities of our supercapacitors to other polymer-based devices. The energy density of a supercapacitor is calculated by the equation $E = CV^2/2$. The power density depends on how quickly the stored energy can be released and is determined according to the equation $P = E/\Delta t$, in which Δt is the discharge time. By employing the stable n-type PCQTh polymer, the operating voltage range covers 3 V, which brings a significant increase in energy density
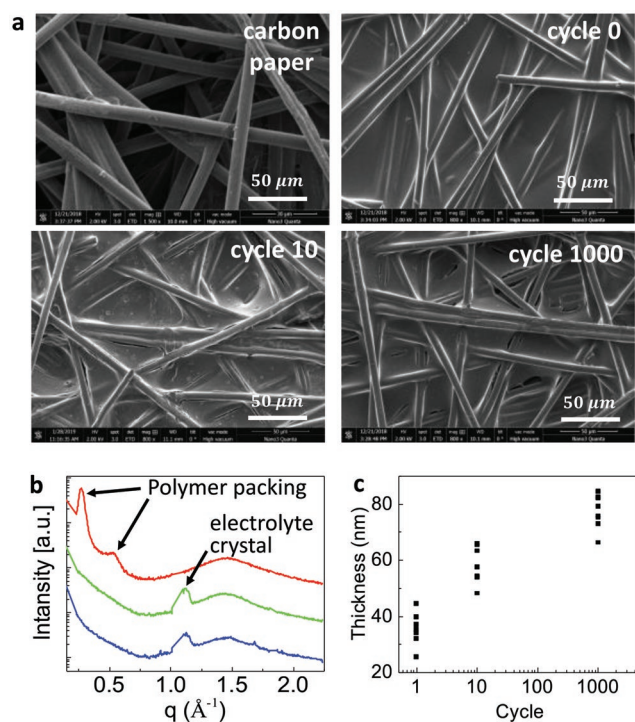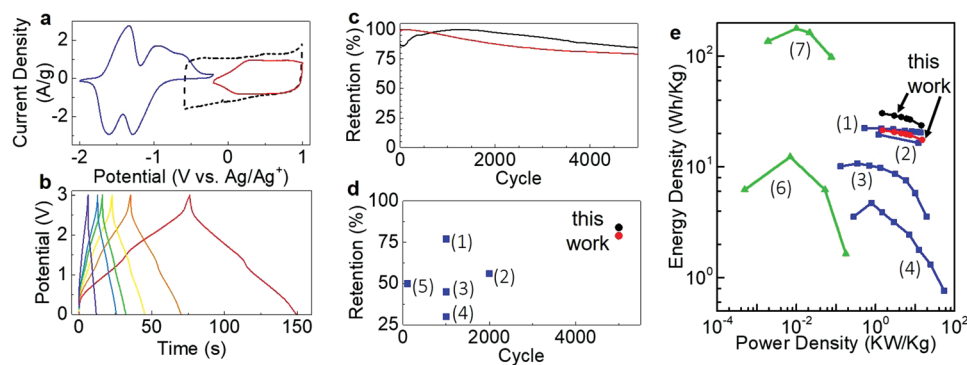

Figure 4. a) Scanning electron microscopy of bare carbon paper electrode and of the drop-casted PCQTh film after various redox cycles. b) X-ray scattering intensity versus scattering vector of the PCQTh film, as deposited (red) and after redox cycle number 10 (green) and 1000 (blue). The curves are offset for clarity. c) Film thicknesses measured at multiple locations on the same sample versus redox cycles.

Figure 5. a) Cyclic voltammetry of the materials used in asymmetric supercapacitors. Blue: PCQTh as an anode. Red: PCQTh as a cathode. Black dashed line: PEDOT:PSS. b) Galvanostatic charge–discharge measurements of the asymmetric supercapacitor at current densities of 1, 2, 3, 4, 5, 10 A g^{-1} (red to purple). c) Capacitance retention of our symmetric (red) and asymmetric (black) supercapacitor. d) Capacitance retention for n-type Faradaic polymers: (1) PMOTP[27]; (2) pCzAQCz[25]; (3) PDEQ[41]; (4) PDDDBT[41]; (5) PBEDOT-iI.[21] e) Comparison of energy density versus power density for polymer supercapacitors, commercial double-layer supercapacitor[41] (6), and commercial lithium battery[41] (7). The symbols in red represent the supercapacitors in this work: black circles (asymmetric electrodes) and red circles (symmetric electrodes).

compared to other lower voltage devices. Our asymmetric supercapacitor reaches a maximum energy density of 30.4 Wh kg^{-1} at 1 A g^{-1} discharge rate. The maximum power density is 14.4 kW kg^{-1} measured at a 10 A g^{-1} discharge rate. At this power delivery, the energy density is 23.6 Wh kg^{-1}. Since we have not yet maximized device surface area in our solid thin film, there is room to increase the specific capacitance. Our results prove the feasibility of using an open-shell conjugated polymer to achieve high-performance anodes. The conducting polymer show performance affected by temperature, for example the capacitance retention decreases faster at 60 °C than at room temperature (Figure S8a, Supporting Information). Nonetheless, with this class of modular DA polymer, it is facile to synthesize and investigate other variants with different side-groups (Figure S8b, Supporting Information), to lower the molecular weight and possibly increase the specific capacitance, energy density, and temperature stability in the future. The conducting polymer also offers mechanical flexibility, which can be characterized and leveraged to build future flexible energy storage devices.

3. Conclusions

This work meets the long-standing challenge of finding a stable n-type material for Faradaic supercapacitors. The use of an open-shell conjugated structure, of which PCQTh is an example, allows the supercapacitors to operate with a 3 V potential window to boost the energy and power densities. The polymer gradually swells with redox cycling, but as the polymer is amorphous, the mechanical changes are well tolerated, and the anode is very stable. For the broad voltage range, the device coulombic efficiency is 99.6%, and to the best of our knowledge, the supercapacitors in this work show the best cycle life among n-type polymeric devices. The polymer shows electrochromic effects, which we leverage to monitor the redox cycling process in situ and distinguish between chemical versus physical degradation processes. The asymmetric supercapacitor with PEDOT:PSS and PCQTh reaches a best-in-class performance of a maximum energy density of 30.4 Wh kg^{-1} at

1 A g^{-1} discharge rate (at the power density of 1.5 kW kg^{-1}). By pairing this PCQTh anode with other energy-dense cathodes and/or with nanostructuring, there are facile paths to further increase device energy and power density in the future. This work highlights the promise of open-shell donor–acceptor polymers as scalable n-type electrodes with long cycle life critical to energy storage applications.

4. Experimental Section

Electrode Fabrication: The detailed synthesis procedure of PCQTh is included in the Supporting Information. Gel permeation chromatography (GPC) at 80 °C in 1,2,4-trichlorobenzene showed a number average molecular weight (M_n) of 23 kg mol^{-1} and dispersity ($Đ$) of 4.00. PCQTh is highly soluble in organic solvents, and a thin-film was prepared by spin-coating a chlorobenzene solution (10 mg mL^{-1}) onto a quartz substrate. The polymer demonstrates an absorption maximum (λ_{max}) of 1.66 µm and optical bandgap (E_g^{opt}) of ≈0.46 eV, as estimated from the absorption onset of the thin film. The PCQTh polymer was dissolved in chloroform at a concentration of 10 mg mL^{-1}. For the electrodes in electrochemical characterization, the polymer solution was drop-casted and spread over 1 cm^2 on the carbon paper current collector (AvCarb MGL190). The mass of dried PCQTh film is roughly 0.5 mg cm^{-2} for the anode, and the mass of cathode active material is matched to the anode charge capacity. For the electrode in GIWAXS characterization, the solution was spin coated at 500 rpm for 1 min on a silicon wafer. The current collector was 50 nm thermally evaporated silver, patterned by a U-shaped shadow mask. The GIWAXS measurement was carried out on the exposed polymer film in the inner region of the U-shaped electrode (Figure S9, Supporting Information). The dried electrolyte sample was prepared by spin coating electrolyte on a silicon wafer. For the electrochromic characterization, the solution was spin coated over ITO transparent conductor on a glass substrate. All electrodes were dried in a nitrogen atmosphere at 200 °C for 10 min.

Electrochemical Characterization: Electrochemical measurements were carried out inside nitrogen glovebox with the BioLogic SP-200 potentiostat. The electrolyte was 0.5 M TEABF$_4$ in propylene carbonate solvent for all the measurements. In three-electrode configuration, nonaqueous Ag/Ag$^+$ reference electrode (CHI 112, CH Instruments) was used as the reference electrode, and carbon paper was the counter electrode.

Electron Spin Resonance (ESR) Spectroscopy: ESR spectra were recorded at room temperature with a Bruker EMX micro EPR spectrometer

with 9.87 GHz (X-band) microwave bridge. The sample (6.6 mg) was evacuated to under vacuum for 12 h before measurement, and the tube was sealed in an N_2-filled glovebox. Spin concentration was obtained by comparison to a standard (2,2-diphenyl-1-picrylhydrazyl, DPPH) powder sample with known spin concentration.

Electrochromic Characterization: The sample was submerged in the electrolyte and then sealed under nitrogen inside a container with an optical window. Optical transmission of the sample is measured using a monochromatic light source modulated at 380 Hz. The photodetector current was amplified by a low-noise amplifier and subsequently recorded by a lock-in amplifier (SRS 510).[42–44] Long-pass filters with cut-off wavelength at 455, 780, and 1100 nm were used to eliminate second-order harmonics in the spectra. During the optical measurements, the sample charge/discharge current was simultaneously monitored by the SP-200 potentiostat.

Grazing Incidence Wide-Angle X-Ray Scattering Characterization: GIWAXS was performed on a Xeuss 2.0 system with a wavelength of 1.54 angstroms and sample-to-detector distance of 153 mm. Samples were measured under vacuum to avoid air scattering. The data was collected with Pilatus 1M detector with an exposure time of 2 h, and later processed using Igor 8 with Nika package and WAXStool software.

Density Functional Theory Calculations: A detailed discussion on the computational calculations can be found in the Supporting Information. All calculations were performed with Gaussian 16 program package using Becke's three-parameter functional B3LYP. Geometry optimizations for model oligomers ($n = 1–4$) were performed in the gas phase with 6–31+G** basis set. After the gas phase geometry optimization, single point energy calculation was done on the minimum energy configuration in the presence of an implicit solvent. Polarizable continuum model (PCM) was used with propylene carbonate as the implicit solvent. An ultrafine grid was used for the numerical integration along with tight convergence criteria for residual force and density matrix. On the bridgehead, the bulky –R group was replaced with –CH_3. Unless otherwise specified, the analysis was done in PCM solvation model.

Supporting Information

Supporting Information is available from the Wiley Online Library or from the author.

Conflict of Interest

The authors declare no conflict of interest.

[1] F. Wang, X. Wu, X. Yuan, Z. Liu, Y. Zhang, L. Fu, Y. Zhu, Q. Zhou, Y. Wu, W. Huang, *Chem. Soc. Rev.* **2017**, *46*, 6816.

[2] Y. Shao, M. F. El-Kady, L. J. Wang, Q. Zhang, Y. Li, H. Wang, M. F. Mousavi, R. B. Kaner, *Chem. Soc. Rev.* **2015**, *44*, 3639.

[3] B. C. Kim, J. Y. Hong, G. G. Wallace, H. S. Park, *Adv. Energy Mater.* **2015**, *5*, 1500959.

[4] A. M. Bryan, L. M. Santino, Y. Lu, S. Acharya, J. M. D'Arcy, *Chem. Mater.* **2016**, *28*, 5989.

[5] X. Lu, M. Yu, G. Wang, Y. Tong, Y. Li, *Energy Environ. Sci.* **2014**, *7*, 2160.

[6] A. L. Balch, K. Winkler, *Chem. Rev.* **2016**, *116*, 3812.

[7] M. F. El-Kady, M. Ihns, M. Li, J. Y. Hwang, M. F. Mousavi, L. Chaney, A. T. Lech, R. B. Kaner, *Proc. Natl. Acad. Sci. USA* **2015**, *112*, 4233.

[8] X. Lu, C. Wang, F. Favier, N. Pinna, *Adv. Energy Mater.* **2017**, *7*, 1601301.

[9] Z. Zhou, T. Liu, A. U. Khan, G. Liu, *Sci. Adv.* **2019**, *5*, eaau6852.

[10] M. Yu, Z. Wang, Y. Han, Y. Tong, X. Lu, S. Yang, *J. Mater. Chem. A* **2016**, *4*, 4634.

[11] X. Xiao, B. Yan, Q. Hu, X. Li, H. Xue, Y. Xu, S. Zheng, H. Pang, *Adv. Energy Mater.* **2017**, *7*, 1602733.

[12] T. B. Schon, B. T. McAllister, P. F. Li, D. S. Seferos, *Chem. Soc. Rev.* **2016**, *45*, 6345.

[13] Z. Niu, P. Luan, Q. Shao, H. Dong, J. Li, J. Chen, D. Zhao, L. Cai, W. Zhou, X. Chen, S. A. Xie, *Energy Environ. Sci.* **2012**, *5*, 8726.

[14] S. H. Park, M. Kaur, D. Yun, W. S. Kim, *Langmuir* **2018**, *34*, 10897.

[15] C. (John) Zhang, L. McKeon, M. P. Kremer, S. H. Park, O. Ronan, A. Seral-Ascaso, S. Barwich, C. Coileáin, N. McEvoy, H. C. Nerl, B. Anasori, *Nat. Commun.* **2019**, *10*, 1795.

[16] M. Meyyappan, M. Koehne, J. Han, *MRS Bull.* **2015**, *40*, 822.

[17] S. Muench, A. Wild, C. Friebe, B. Häupler, T. Janoschka, *Chem. Rev.* **2016**, *116*, 9438.

[18] Y Joo, V. Agarkar, S. H. Sung, B. M. Savoie, B. W. Boudouri, *Science* **2018**, *359*, 1391.

[19] S. Wang, F. Li, A. D. Easley, J. L. Lutkenhaus, *Nat. Mater.* **2019**, *18*, 69.

[20] Y. Morita, S. Nishida, T. Murata, M. Moriguchi, A. Ueda, M. Satoh, K. Arifuku, K. Sato, T. Takui, *Nat. Mater.* **2011**, *10*, 947.

[21] L. A. Estrada, D. Y. Liu, D. H. Salazar, A. L. Dyer, J. R. Reynolds, *Macromolecules* **2012**, *45*, 8211.

[22] D. F. Zeigler, S. L. Candelaria, K. A. Mazzio, T. R. Martin, E. Uchaker, S. L. Suraru, L. J. Kang, G. Cao, C. K. Luscombe, *Macromolecules* **2015**, *48*, 5196.

[23] T. B. Schon, P. M. Dicarmine, D. S. Seferos, *Adv. Energy Mater.* **2014**, *4*, 1.

[24] B. T. McAllister, T. B. Schon, P. M. DiCarmine, D. S. Seferos, *Polym. Chem.* **2017**, *8*, 5194.

[25] H. Zhang, M. Yao, J. Wei, Y. Zhang, S. Zhang, Y. Gao, J. Li, P. Lu, B. Yang, Y. Ma, *Adv. Energy Mater.* **2017**, *7*, 1701063.

[26] T. Van Voorhis, Z. Lin, M. D. Peeks, S. Lin, T. M. Swager, P. Wang, *J. Am. Chem. Soc.* **2018**, *140*, 10881.

[27] X. Ju, L. Kong, J. Zhao, G. Bai, *Electrochim. Acta* **2017**, *238*, 36.

[28] A. E. London, H. Chen, M. A. Sabuj, B. A. Zhang, J. Tropp, Y. Liu, X. Gu, B. Wong, N. Rai, M. K. Bowman, J. A. Azoulay, *Sci. Adv.* **2019**, *5*, eaav2336.

[29] J. Rivnay, S. Inal, B. A. Collins, M. Sessolo, E. Stavrinidou, X. Strakosas, C. Tassone, D. M. Delongchamp, G. G. Malliaras, *Nat. Commun.* **2016**, *7*, 11287.

[30] Y. Joo, L. Huang, N. Eedugurala, A. E. London, A. Kumar, B. M. Wong, B. W. Boudouris, J. D. Azoulay, *Macromolecules* **2018**, *51*, 3886.

[31] M. D. Stoller, R. S. Ruoff, *Energy Environ. Sci.* **2010**, *3*, 1294.

[32] C. Peng, D. Hu, G. Z. Chen, *Chem. Commun.* **2011**, *47*, 4105.

[33] V. Augustyn, P. Simon, B. Dunn, *Energy Environ. Sci.* **2014**, *7*, 1597.

[34] C. G. Wu, M. I. Lu, S. J. Chang, C. S. Wei, *Adv. Funct. Mater.* **2007**, *17*, 1063.

**ADVANCED
SCIENCE NEWS**

www.advancedsciencenews.com

**ADVANCED
ENERGY
MATERIALS**

www.advenergymat.de

[35] C. L. Gaupp, D. M. Welsh, R. D. Rauh, J. R. Reynolds, *Chem. Mater.* **2002**, *14*, 3964.

[36] Y. Shi, L. Peng, Y. Ding, Y. Zhao, G. Yu, *Chem. Soc. Rev.* **2015**, *44*, 6684.

[37] K. Kwon, T. N. Ng, *Org. Electron.* **2014**, *15*, 294.

[38] E. Smela, N. Gadegaard, *J. Phys. Chem. B* **2001**, *105*, 9395.

[39] L. M. Santino, Y. Lu, S. Acharya, L. Bloom, D. Cotton, A. Wayne, J. M. D'Arcy, *ACS Appl. Mater. Interfaces* **2016**, *8*, 29452.

[40] A. M. Österholm, D. E. Shen, A. L. Dyer, J. R. Reynolds, *ACS Appl. Mater. Interfaces* **2013**, *5*, 13432.

[41] P. M. Dicarmine, T. B. Schon, T. M. McCormick, P. P. Klein, D. S. Seferos, *J. Phys. Chem. C* **2014**, *118*, 8295.

[42] Z. Wu, W. Yao, A. E. London, J. D. Azoulay, T. N. Ng, *ACS Appl. Mater. Interfaces* **2017**, *9*, 1654.

[43] Z. Wu, Y. Zhai, W. Yao, N. Eedugurala, S. Zhang, L. Huang, X. Gu, J. D. Azoulay, T. N. Ng, *Adv. Funct. Mater.* **2018**, *28*, 1805738.

[44] W. Yao, Z. Wu, E. Huang, L. Huang, A. E. London, Z. Liu, J. D. Azoulay, T. N. Ng, *ACS Appl. Electron. Mater.* **2019**, *1*, 660.

1902806 (8 of 8)